ADVANCED FUNCTIONAL MATERIALS

FULL PAPER

DOI: 10.1002/adfm.200500849

Monomolecular-Layer $Ba_5Ta_4O_{15}$ Nanosheets: Synthesis and Investigation of Photocatalytic Properties**

By *Tong-Guang Xu*, *Chuan Zhang*, *Xiang Shao*, *Kai Wu*, and *Yong-Fa Zhu**

Monomolecular-layer perovskite $Ba_5Ta_4O_{15}$ nanosheets with hexagonal structure have been synthesized by a hydrothermal method. The thickness of the nanosheets is about 1.1 nm, which corresponds to a monolayer of $Ba_5Ta_4O_{15}$ molecules, with the lateral size ranging from 50 to 200 nm. The optimal conditions for the formation of the nanosheets are maintaining the reactants above 270 °C for 24 h. A dissolution–recrystallization mechanism is suggested based on observations of the factors that influence nanosheet formation, such as reaction time, temperature, and basicity. Formation of $Ba_5Ta_4O_{15}$ nanosheets takes precedence over other nanostructures under high concentrations of OH^- because the hindering effect of OH^- ions on the *c*-axis growth is strong. Thus, the extended growth rate of polyhedrons on one monolayer is much faster than the superposition rate of the monolayer, and the crystal grows more easily along the *a*- and *b*-planes. The $Ba_5Ta_4O_{15}$ nanosheets show a high photocatalytic activity in the degradation of Rhodamine B and gaseous formaldehyde. The layered perovskite probably affects the photocatalytic activity by promoting the charge separation and delocalization of photogenerated electrons and holes.

1. Introduction

Nanosheets can be regarded as a new class of materials combining features such as single-crystalline quality, high crystallinity, well-defined chemical composition, and extremely high anisotropy with ultrathin thickness.[1] These unusual characteristics result in distinctive physicochemical properties, as compared to conventional nanocrystallites and bulk materials. A wide range of applications can be envisaged for this new class of materials, particularly in the areas of nanoscience and nanomaterials.[2] Nanosheets derived from functional layered materials are particularly interesting from the materials synthesis viewpoint because they can be used as building blocks to construct a wide variety of nanostructured systems. Multilayer ultrathin films of different compositions and architectures have been fabricated.[3] For example, Sato and co-workers have prepared semiconductor-pillared layered titanates.[4] Mallouk and co-workers have carried out an extensive study of the exfoliation of various types of layered niobates and other related materials. They observe the formation of nanosheets in perovskite-related architectures, especially in $Ca_2Nb_3O_{10}$, as well as the formation of scrolls and tubular structures from Nb_6O_{17} nanosheets.[5] Recently, nanosheets of $K_4Nb_6O_{17}$, $HTiNbO_5$, HNb_3O_8, and $HCa_2Nb_3O_{10}$ have attracted great attention due to their potential application in advanced materials based on their photoactive properties.[6] The large inner surface of these layered materials may potentially be available for various catalytic reactions if the reactant molecules can be intercalated inside the structures. Such reactions will effectively promote photocatalytic hydrogen evolution since the recombination between photoinduced electrons and holes is depressed by electron transfer to a layered host.

These nanosheets are usually synthesized by delaminating precursor layered-crystals into elementary layers by soft-chemical methods,[7] such as ion-exchange, exfoliation/delamination, etc., wherein complicated processes and very high temperatures (1073–1273 K) are necessary. In addition, the desired product is obtained very slowly, requiring a high concentration of organic compounds. Consequently, the large-scale production of low-cost materials is almost impossible.

Niobates and tantalates are useful in photochemical and photocatalytic applications owing to their semiconducting nature. Tantalates possess conduction bands consisting of a Ta_{5d} orbital located at a more negative position than titanates (Ti_{3d}) and niobates (Nb_{4d}), which have conduction bands at a higher potential. A variety of mixed metal oxides containing closed-shell Ta^{5+} transition-metal ions have been studied recently. The results show that some alkali and alkaline-earth tantalates, such as $LiTaO_3$, $KTaO_3$, and $NaTaO_3$, as well as $SrTa_2O_6$, $CaTa_2O_6$, $BaTa_2O_6$, $Sr_2Ta_2O_7$, $K_3Ta_3Si_2O_{13}$, and $A_4Ta_xNb_{6-2x}O_{17}$ (A = K, Rb), have high photocatalytic activities.[8] These tantalates are good photocatalysts not only for splitting water into H_2, but also for the degradation of environmental pollutants.

The development of a wide range of nanoscale structures from the materials mentioned above is very important for the design of nanodevices possessing sophisticated functionality. This work describes details of the hydrothermal synthesis of $Ba_5Ta_4O_{15}$ nanosheets at low temperature without any ion-ex-

[*] Prof. Y.-F. Zhu, Dr. T.-G. Xu, Dr. C. Zhang
Department of Chemistry, Tsinghua University
Beijing 100084 (P.R. China)
E-mail: zhuyf@mail.tsinghua.edu.cn
Dr. X. Shao, Prof. K. Wu
College of Chemistry, Peking University
Beijing 100084 (P.R. China)

[**] This work was supported by the Chinese National Science Foundation (20433010 and 20571047).

change or exfoliation. The nanosheets have been prepared in a single-crystalline phase without using any template. The influence of various factors on the formation process and the effects of the preparation temperature and time on the photocatalytic activities of these materials have been investigated systematically. The $Ba_5Ta_4O_{15}$ nanosheets show a higher photocatalytic activity for the degradation of pollutants under UV light, as compared to bulk $Ba_5Ta_4O_{15}$ samples.

2. Results and Discussion

2.1. Formation of $Ba_5Ta_4O_{15}$ Nanosheets

The reaction temperature and the concentration of $Ba(OH)_2$ greatly influence the growth of the $Ba_5Ta_4O_{15}$ nanosheets. Figure 1 shows the X-ray diffraction (XRD) patterns of some samples prepared at different temperatures. When the reactants are maintained at 250 °C for 24 h, the resulting sample is amorphous. However, several sharp peaks are observed after heating the reactants at 260 °C for 24 h. These peaks can be attributed to crystalline $Ba_5Ta_4O_{15}$, based on standard diffraction patterns of $Ba_5Ta_4O_{15}$ (Joint Committee on Powder Diffraction Standards (JCPDS) 72-0631). This indicates that the $Ba_5Ta_4O_{15}$ crystal structure could be obtained at 260 °C after 24 h by this method. However, the crystal phase obtained is not perfect and other phases are also seen to coexist. Prolonging the reaction time (from 24 to 48 h) does not significantly improve the purity. When the reaction temperature is increased to 270 or 280 °C, the XRD peaks become much sharper and more intense, because of the successful production of crystalline $Ba_5Ta_4O_{15}$. Therefore, the reaction temperature needs to be optimized for the formation of nanosheets. We have found that the optimum temperature is in the 270 to 290 °C range. We also observe that the XRD patterns of $Ba_5Ta_4O_{15}$ basically consist of the ($hk0$) basal series and ($h0l$) and ($0kl$) reflections; the (001) reflection peak at 7.5° is not observed at all times, indicating the absence of 3D order. Well-crystallized $Ba_5Ta_4O_{15}$ can also be obtained by a solid-state reaction (SSR) at 1100 °C and serves as a standard for comparison to the materials obtained by the hydrothermal method. Furthermore, the intensity ratio of the (110)/(013) peaks for hydrothermally synthesized $Ba_5Ta_4O_{15}$ is much higher than that for $Ba_5Ta_4O_{15}$ prepared by the SSR; also, the peaks are broadened in the tantalate nanosheets, as compared to the SSR tantalates, suggesting that the as-synthesized $Ba_5Ta_4O_{15}$ might have a preferential growth orientation along the (110) plane. This is further confirmed by selected area electron diffraction (SAED) and high-resolution transmission electron microscopy (HRTEM) studies.

The transformation of $Ba_5Ta_4O_{15}$ has been further studied by Raman spectroscopy (Fig. 2). Four characteristic peaks at 251, 625, 712, and 843 cm^{-1} can be found in pure Ta_2O_5. When the reaction is carried out at 250 °C for 24 h, the peaks corresponding to Ta_2O_5 disappear and are replaced by a new weak and broad peak at about 630 cm^{-1}, indicating that the Ta_2O_5 has reacted with $Ba(OH)_2$. However, crystalline $Ba_5Ta_4O_{15}$ has still not been formed. A large red-shift occurs relative to the peaks of Ta_2O_5 as the temperature is increased to 260 °C. After the reactants are kept at 270 °C for 24 h, perfectly crystalline $Ba_5Ta_4O_{15}$ is obtained, as evidenced by characteristic peaks at 316, 441, 641, 785, and 861 cm^{-1}. The Raman spectrum of the product obtained at 280 °C is similar to that of the sample prepared at 270 °C. In the absence of polarization analysis, it is difficult to make an unequivocal assignment of all the peaks. However, we can interpret the Raman spectra according to Doba et al. as follows:[9a] the mid-energy Raman bands (200–450 cm^{-1}) generally correspond to O–Ta–O bending vibrations in the TaO_6 octahedra; pure skeletal modes involving Ta–O–Ta bending coordinates in different types of polyhedra may also

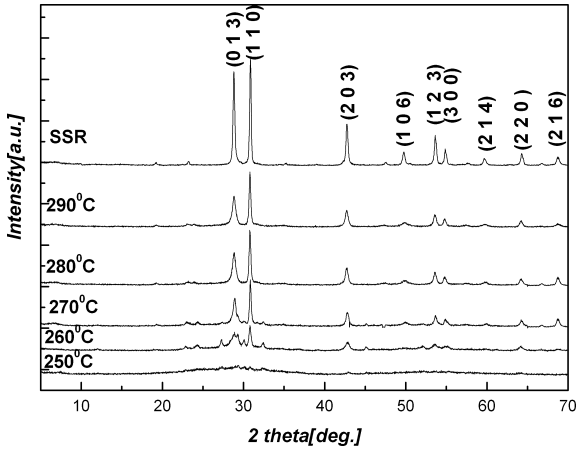

Figure 1. XRD patterns of samples prepared by heating Ta_2O_5 and 0.1 M $Ba(OH)_2$ for 24 h at different temperatures: 250, 260, 270, 280, and 290 °C (molar ratio of $Ba(OH)_2/Ta_2O_5 = 5:2$). The XRD pattern of the product of the solid-state reaction (SSR) is also shown.

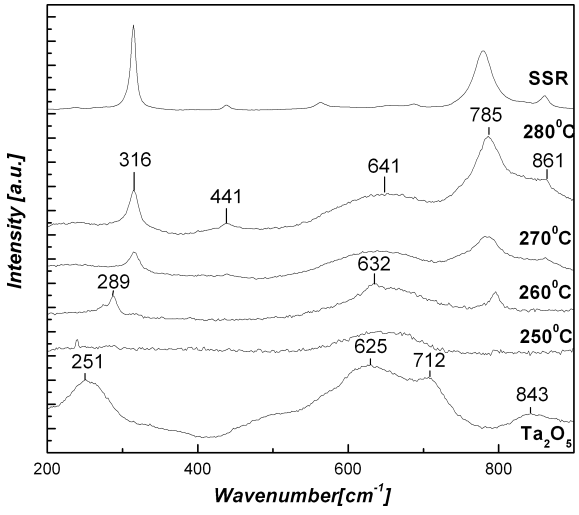

Figure 2. Raman spectra for samples prepared by the hydrothermal method and the SSR; hydrothermal conditions: $Ba(OH)_2/Ta_2O_5 = 5:2$, 24 h, and different temperatures: 250, 260, 270, and 280 °C.

contribute to several of these bending modes. The higher energy bands (450–1000 cm^{-1}) at 785 and 861 cm^{-1} may be associated with coupled modes, primarily related to the stretching of the various Ta–O bonds. The band at 785 cm^{-1} is likely to be related to atomic motions of the corner-sharing oxygen atoms.[9b] The higher wavenumber bands may arise from higher polyhedral distortions. The distortion of the TaO_6 octahedrons is likely to be very small, and the structure deviation is not large enough to be detected by XRD. The high-energy band corresponding to Ta–O bonds gradually shifts to higher energies until a new peak emerges at 641 cm^{-1}, which may be substantially associated with Ba–O vibrations. This also implies that crystalline $Ba_5Ta_4O_{15}$ is gradually formed as the reaction temperature increases. The Raman spectra of the SSR-synthesized $Ba_5Ta_4O_{15}$ is also shown in Figure 2; the main peaks are more intense and show a better signal to noise ratio, as compared with $Ba_5Ta_4O_{15}$ samples obtained by the hydrothermal method, indicating the good crystallinity and relatively low concentration of defects in SSR $Ba_5Ta_4O_{15}$. From the above results, the optimal reaction temperature for the hydrothermal synthesis of $Ba_5Ta_4O_{15}$ is at least 270 °C.

Figure 3 shows the XRD patterns for four samples heated at 270 °C for 24 h with varying ratios of $Ba(OH)_2/Ta_2O_5$ (Ba/Ta) ranging from 1:2 to 10:1. At low $Ba(OH)_2$ concentrations ($Ba(OH)_2/Ta_2O_5 = 1:2$, 1:1), the resulting product is not as well

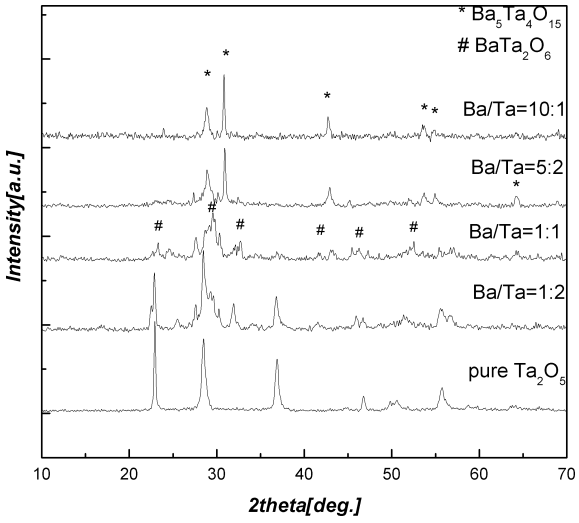

Figure 3. XRD patterns for samples produced with different $Ba(OH)_2/Ta_2O_5$ ratios: 1:2, 1:1, 5:2, and 10:1. The reaction was carried out for 24 h at 270 °C.

crystallized, and unreacted Ta_2O_5 and $BaTa_2O_6$-type phases (JCPDS 20-0146) are also obtained. For samples prepared at ratios ranging from 5:2 to 10:1, pure $Ba_5Ta_4O_{15}$ is obtained as the only stable phase. The crystallite size for the powders is about 50–60 nm and 80–90 nm, respectively, suggesting that the crystallite size increases with the $Ba(OH)_2$ concentration. TEM images of these four samples are shown in Figure 4. It can be seen that the sample formed at $Ba(OH)_2/Ta_2O_5 = 1:2$ (Fig. 4a) is quite different from the others. At this ratio, the

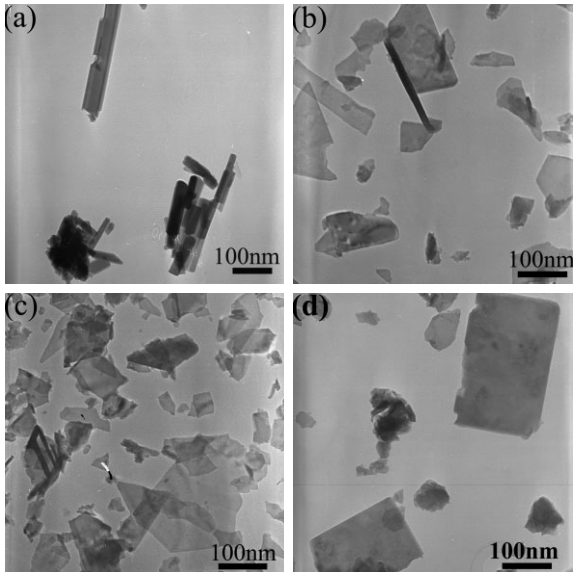

Figure 4. TEM images of products obtained for different $Ba(OH)_2/Ta_2O_5$ ratios: a) 1:2, b) 1:1, c) 5:2, and d) 10:1. The reaction was carried out for 24 h at 270 °C.

product consists primarily of nanorods with diameters ranging from 20–40 nm, with lengths in the 100 to 300 nm range. The sample formed at $Ba(OH)_2/Ta_2O_5 = 1:1$ (Fig. 4b) is composed of nanosheets, as well as a few nanorods with diameters of 10 nm and lengths ranging up to 150 nm. However, the nanosheets in this sample display an irregularly shaped morphology with the particle size ranging from 40 to 150 nm. When the concentration of $Ba(OH)_2$ is 0.1 M ($Ba(OH)_2/Ta_2O_5 = 5:2$), the nanorods disappear and only irregular rectangular $Ba_5Ta_4O_{15}$ nanosheets ranging from 30 to 150 nm in size can be seen, as shown in Figure 4c. Upon further increasing the concentration of OH^- to 0.4 M ($Ba(OH)_2/Ta_2O_5 = 10:1$), the obtained $Ba_5Ta_4O_{15}$ product (Fig. 4d) is seen to be quite similar to the sample shown in Figure 4c, though now the nanosheets appear to be larger and more regular. These results imply that for the formation of nanosheets, a molar ratio of $Ba(OH)_2/Ta_2O_5$ above 5:2 is most suitable, and that the formation of $Ba_5Ta_4O_{15}$ nanosheets is favored by higher concentrations of OH^-.

In order to understand the growth mechanism of the $Ba_5Ta_4O_{15}$ nanosheets, the reaction time is varied from 0 to 48 h (Fig. 5). No $Ba_5Ta_4O_{15}$ crystal phase is formed when the reaction is carried out at 270 °C for only 2 or 4 h; however, the reflections corresponding to the Ta_2O_5 reactant become weaker in intensity. After carrying out the reaction at 270 °C for 12 h, the crystalline phase of $Ba_5Ta_4O_{15}$ starts to emerge. However, the obtained crystal phase is not perfect and is still mostly amorphous. All the diffraction peaks of $Ba_5Ta_4O_{15}$ are observed after keeping the reactants at 270 °C for 24 h. The XRD peaks become much sharper upon prolonging the reaction time.

Figure 6 shows the TEM images of five samples taken at different times: a) 0 h, b) 2 h, c) 4 h, d) 12 h, and e) 24 h during the hydrothermal reaction at 270 °C; for comparison, the $Ba_5Ta_4O_{15}$ particles obtained by the SSR are shown in Fig-

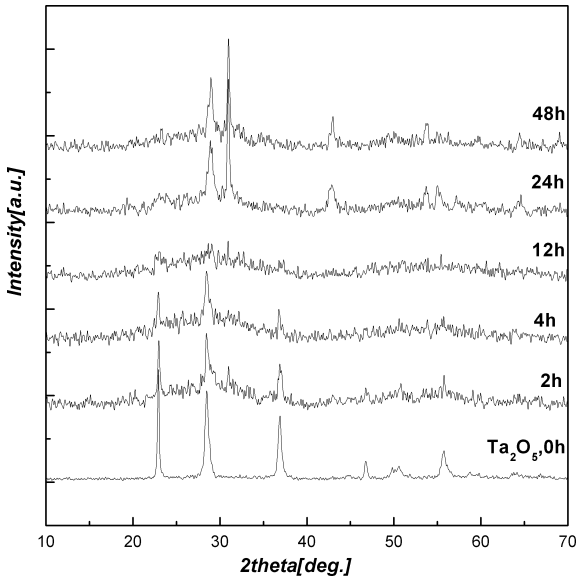

Figure 5. XRD patterns of samples obtained at 270 °C after different preparation times: 0–48 h, with $Ba(OH)_2/Ta_2O_5 = 5{:}2$ (molar ratio).

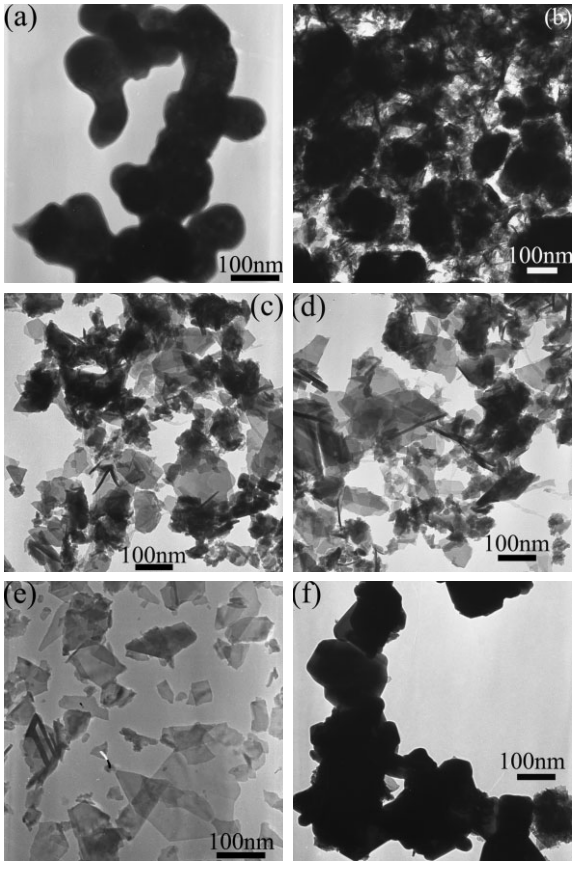

Figure 6. TEM images of samples prepared at 270 °C by the hydrothermal method for different times: a) 0 h, b) 2 h, c) 4 h, d) 12 h, and e) 24 h. f) TEM image of the SSR $Ba_5Ta_4O_{15}$ sample.

ure 6f. These micrographs clearly demonstrate the evolution of $Ba_5Ta_4O_{15}$ nanostructures from nanoparticles to nanosheets. The growth process of the $Ba_5Ta_4O_{15}$ nanosheets can be described as follows: the initial Ta_2O_5 consists mainly of sphere-like nanoparticles with diameters ranging from 50–100 nm (Fig. 6a). After 2 h of the reaction, the sample morphology remain similar to the precursor with an ill-defined shape (Fig. 6b). About 4 h later, the black aggregated nanoparticles become smaller and laminar structures can be observed among the irregular particles, as shown in Figure 6c. When the reaction time is increased to 12 h, the particles disappear and some nanosheets start to emerge (Fig. 6d). When the reaction time exceeds 24 h, irregularly shaped nanosheets can be seen exclusively with an average dimension of ca. 60 nm (Fig. 6e). This means that the growth of $Ba_5Ta_4O_{15}$ crystals advances with the passage of time. The formation pathway for bulk $Ba_5Ta_4O_{15}$ is quite different from the dissolution–recrystallization process for $Ba_5Ta_4O_{15}$ nanosheets, instead the SSR $Ba_5Ta_4O_{15}$ is formed by homogeneous nucleation and conglomeration under high temperature. Thus, the SSR $Ba_5Ta_4O_{15}$ particles (300 nm) are much larger than the nanosheets (Fig. 6f). Overall, we have found that the optimal conditions for the hydrothermal synthesis of $Ba_5Ta_4O_{15}$ nanosheets involve the reaction of $Ba(OH)_2$ and Ta_2O_5 at 270 °C for 24 h with a molar ratio of $Ba(OH)_2/Ta_2O_5 = 5{:}2$.

2.2. Characterization of $Ba_5Ta_4O_{15}$ Nanosheets

Figure 7a shows a TEM image of the $Ba_5Ta_4O_{15}$ nanosheets. The sample is composed of very thin crystallites with uniform and faint contrast, as is characteristic of nanosheets. The TEM image allows one to identify individual nanosheet crystallites. There are some spots where two crystallites are overlapped and the contrast is approximately doubled relative to that of

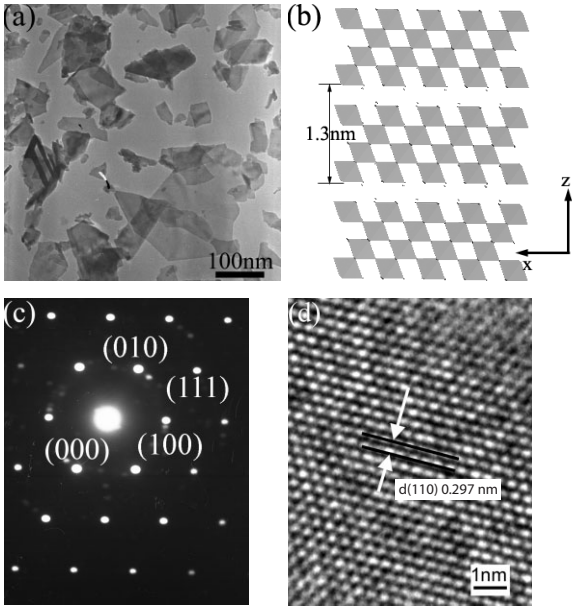

Figure 7. TEM images and SAED patterns of $Ba_5Ta_4O_{15}$ nanosheets: a) TEM image of $Ba_5Ta_4O_{15}$ nanosheets obtained at $Ba(OH)_2/Ta_2O_5 = 5{:}2$, 270 °C, 24 h. b) Schematic structure of layered $Ba_5Ta_4O_{15}$ nanosheets, where the layer distance is 1.13 nm, and c) SAED pattern obtained from one nanosheet. d) HRTEM image of a $Ba_5Ta_4O_{15}$ nanosheet.

other sections. These features imply that the crystallites are very thin and probably unilamellar. The typical sample dimensions range from 50 to 150 nm. From the schematic depiction of the layered $Ba_5Ta_4O_{15}$ nanosheets shown in Figure 7b, we can see that the layered $Ba_5Ta_4O_{15}$ structure consists of five close-packed oxygen and barium layers, with the Ta^{5+} ions occupying 80 % of the octahedral sites. The strata of the TaO_6 polyhedra are oriented perpendicular to the *c*-axis and are separated from each other by regions containing only BaO_{12} polyhedra. The TaO_6 octahedra are combined via corner sharing to produce 2D arrays and the thickness of a monolayer unit cell of $Ba_5Ta_4O_{15}$ is 1.3 nm. Figure 7c shows the SAED pattern of a randomly selected single nanosheet, obtained by focusing the incident electron beam along the (001) zone axis. The SAED pattern shows a hexagonal array of sharp spots, and can be indexed as hexagonal $Ba_5Ta_4O_{15}$, which is consistent with the XRD results. The observed lattice spacings of 0.29 nm and 0.31 nm can be attributed to the (110) and (013) Bragg reflections of hexagonal $Ba_5Ta_4O_{15}$, respectively. SAED patterns obtained for different individual nanosheets essentially show the same features, indicating that the $Ba_5Ta_4O_{15}$ nanosheets have a single-crystalline structure. HRTEM images provide further evidence for the hexagonal structure of the $Ba_5Ta_4O_{15}$ nanosheets (Fig. 7d). Furthermore, the HRTEM images reveal that the interplanar distance along the growth axis is 0.297 nm. This can be indexed to the (110) plane of hexagonal $Ba_5Ta_4O_{15}$, confirming that the (110) direction is the preferred growth direction for the growth of the nanosheets. The molar ratios of the $Ba_5Ta_4O_{15}$ nanosheets have been examined by energy dispersive X-ray (EDX) analysis and X-ray fluorescence (XRF). The elemental Ba/Ta/O molar ratio has been determined to be 4.7:4:15.2 in the nanosheets, which is quite close to ideal value for $Ba_5Ta_4O_{15}$.

The thickness of the $Ba_5Ta_4O_{15}$ nanosheets has been measured by atomic force microscopy (AFM), as exemplified by a typical image of nanosheets deposited on a mica wafer substrate (Fig. 8). The observed features display lateral dimensions consistent with the morphology of the nanosheets. A height difference of 1.08 ± 0.05 nm is frequently encountered between the nanosheet terrace and the bare substrate surface, as depicted in the roughness profile. This average height is very close to the *c*-axis lattice parameter ($c = 1.3$ nm). The thickness distribution of the $Ba_5Ta_4O_{15}$ film is shown in Figure 8c. The histogram exhibits a sharp and predominant population at a height of 1.0 nm, corresponding to a single unit cell thickness for $Ba_5Ta_4O_{15}$. We also observe that the $Ba_5Ta_4O_{15}$ nanosheets aggregate together to form multilayer nanosheets when deposited on a silicon wafer; the thickness of these multilayers range from 4–6 nm, corresponding to 3–5 unit cells of $Ba_5Ta_4O_{15}$. Multilayers are formed on silicon substrates because the attractive forces between the nanosheets are stronger than the force between the silicon wafer and the nanosheets.

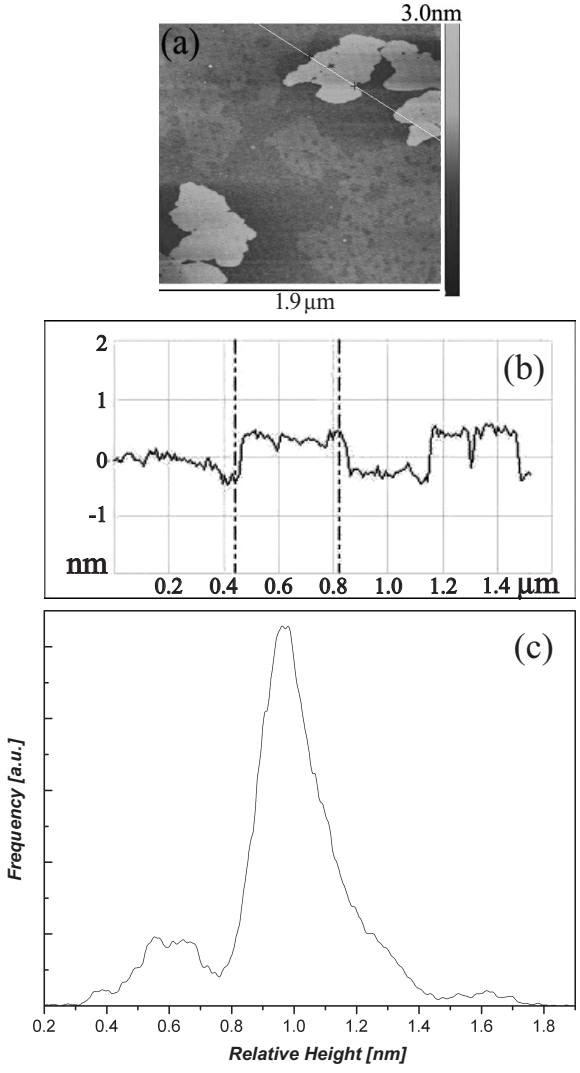

Figure 8. AFM image of $Ba_5Ta_4O_{15}$ nanosheets deposited on a mica wafer, b) roughness profile, and c) histogram of relative height for the $Ba_5Ta_4O_{15}$ monolayer film on the mica substrate.

2.3. Proposed Mechanism

Based on the experimental data, it can be concluded that the growth of the nanosheets is not catalyst assisted since the only source material used in this study are pure transition-metal oxides and alkaline-earth hydroxide crystals. The nanosheet formation process can be explained by a dissolution–recrystallization mechanism. It is well known that the most important factor affecting the growth of single crystals in solution is the solubility of the solute. Under normal conditions, crystalline Ta_2O_5, which consists of aggregates with a primary size of 50–100 nm, is insoluble in water. When used as a reactant under hydrothermal conditions, the interaction between these small particles is broken. Thus, these powders can be partly dissolved and hydroxylated into the corresponding hydroxide, i.e., $Ta_2O_5 \cdot x\,H_2O$ or $Ta(OH)_5$, under high temperature and high pressure. Then, a variety of hydroxylated Ta–O ionic groups are formed under strongly alkaline conditions. These hydroxylated Ta–O ions are the building blocks for the growth of $Ba_5Ta_4O_{15}$. When the concentration of Ba^{2+} reaches or exceeds supersaturation, $Ba_5Ta_4O_{15}$ crystallites begin to nucleate. As soon as the $Ba_5Ta_4O_{15}$ nanosheets are formed, they break off

from the outer layer of the hydroxide into solution, whereas the inner hydroxide layer continues to react with the surrounding $Ba(OH)_2$. In the early stages, the intermediate samples show the coexistence of small laminar structures and irregular crystalline nuclei. As the reaction progresses, the nanoparticles vanish and larger nanosheets are formed. For a crystal with an anisotropic crystal structure, the crystal face containing the corner of the coordination polyhedron at the interface possesses the fastest growth rate. Crystal faces with the edge and face of the coordination polyhedron occurring at the interface represent the second fastest and the slowest growth directions, respectively.[10] Due to the enhanced growth of polyhedrons along the perovskite-like layers ($Ta_4O_{15}^{5-}$), as compared with the stacking of slabs connected by Ba^{2+}, under the present hydrothermal conditions, the crystallites tend to grow along the *a*- and *b*-axes, because of their lower chemical potentials, as compared to the *c*-axis. This hypothesis has been confirmed by HRTEM results. Banfield and co-workers have provided strong evidence that some natural minerals and synthetic nanocrystals grow through a mechanism involving the oriented attachment of nanocrystals.[11] In a layered chemical compound, the interaction energy between atoms in neighboring layers is usually less than the interaction energy between atoms in the same layer. Thus, the growth of the nanosheets predominately occurs at the edges of the individual layers, rather than through the initiation of a new layer. During the spontaneous crystallization and rapid growth of layers, it is possible that the widths of the different layers vary,[12] and thus uniform nanosheets cannot be obtained in this situation. During this process, the precursors for further crystal growth are bulk particles rather than ionic species, which is notably different from previous reports based on homogeneous nucleation and solution-growth processes.[11,13]

In the hydrothermal process, the hydroxyl-ion activity is critical for promoting the formation of the perovskite phase. During the reaction process, the excess $Ba(OH)_2$ serves both as a reactant and as a mineralizer.[14] The differences between the morphologies of the four samples (Fig. 4a–d) can be attributed to the reaction kinetics. From a kinetics perspective of crystal growth, it has to be assumed that the growth mechanism is mainly concerned with the formation of growth units and the incorporation of growth units into the crystal lattice at the interface. In the supersaturated solution, the growth unit is the complex formed by the OH^- ions, whose coordination number is equal to that of the cation in the crystal that is about to be formed. During crystallization, the growth unit is shielded by OH^- ions, which hinders the growth of crystals.[13] Thus, due to the shielding effect of OH^- ions at the interface, the growth rate of various faces gets slowed down. One can conclude that the binding energy of the OH^- ligand at the different interfaces is different, and thus the hindrance effect exerted by the OH^- ions is different at different interfaces. The larger the binding energy of the OH^- ligand present at the interface, the larger is the hindrance effect exerted by the OH^- ions at the interface. In general, therefore, this effect results in differential rates of crystal growth on each axis. In the case of $Ba_5Ta_4O_{15}$, the hindering effect of the OH^- ions influences the *c*-axis more than the *a*- and *b*-axes. Consequently, the crystal can grow more easily along the *a*- and *b*-planes, and the morphology of the nanosheet sample prepared under higher concentrations of $Ba(OH)_2$ is consistent with growth modified by this shielding effect.

2.4. Photocatalytic Properties of the $Ba_5Ta_4O_{15}$ Nanosheets

The photocatalytic activity of the $Ba_5Ta_4O_{15}$ nanosheets has been studied in photodegradation reactions of Rhodamine B solution (RhB) and gaseous formaldehyde under UV irradiation. Figure 9a shows the degradation curves for RhB in the presence of $Ba_5Ta_4O_{15}$ nanosheets prepared at different temperatures (the reaction time for preparing the nanosheets is kept constant at 24 h). As shown in the figure, the apparent reaction constant for sheets prepared by a 24 h reaction at 250 °C is 0.01266 min^{-1}. The photocatalytic activity of the samples increases with the reaction temperature used for preparing the nanosheets, owing to the better crystalline order of structures formed at higher temperatures. When the synthesis temperature is 260 or 270 °C, the photocatalytic activity of the fabricated nanosheets is significantly increased and the apparent reaction constants are 0.02055 and 0.02816 min^{-1}, respectively. The model substrate RhB and gaseous formaldehyde are completely degraded upon being subjected to UV irradiation for 60 min in the presence of $Ba_5Ta_4O_{15}$ nanosheets prepared at 270 °C (Fig. 9b). This photocatalytic performance is ten times better than that of SSR $Ba_5Ta_4O_{15}$ particles. However, compared with TiO_2 (P25, Degussa), these samples have a lower photocatalytic activity; this can be explained by the better dispersion and higher absorption capacity of P25, as compared to the $Ba_5Ta_4O_{15}$ samples prepared here. Nanosheets prepared at 280 and 290 °C however show reduced photocatalytic activity and lower apparent reaction constants. The degradation of formaldehyde over the $Ba_5Ta_4O_{15}$ nanosheets is shown in Figure 9d. Samples prepared at different temperatures show similar photocatalytic performance, and gaseous formaldehyde is completely degraded over the tantalate nanosheets within 40 min under UV irradiation. The photocatalytic activity of the nanosheets is about twice that of SSR tantalates for the decomposition of formaldehyde. Figure 10a shows the degradation of RhB by samples prepared at 270 °C using various reaction times. For samples synthesized using prolonged reaction times, the crystal structure becomes more perfect, resulting in increased photoactivity. When the reaction time is increased to 24 h, the photocatalytic performance of the nanosheets reaches a peak. Further increasing the reaction time for the preparation of the nanosheets does not yield any further improvements in photocatalytic activity, and the apparent reaction constant for nanosheets prepared by a 48 h reaction is only 0.01631 min^{-1}.

As is well known, the photocatalytic activity of a semiconductor is dominated by many factors, including the crystal structure, bandgap, lifetime of the photoinduced charge carriers, etc. The photocatalytic performance is not outstanding here because the crystal structure is not well formed due to the

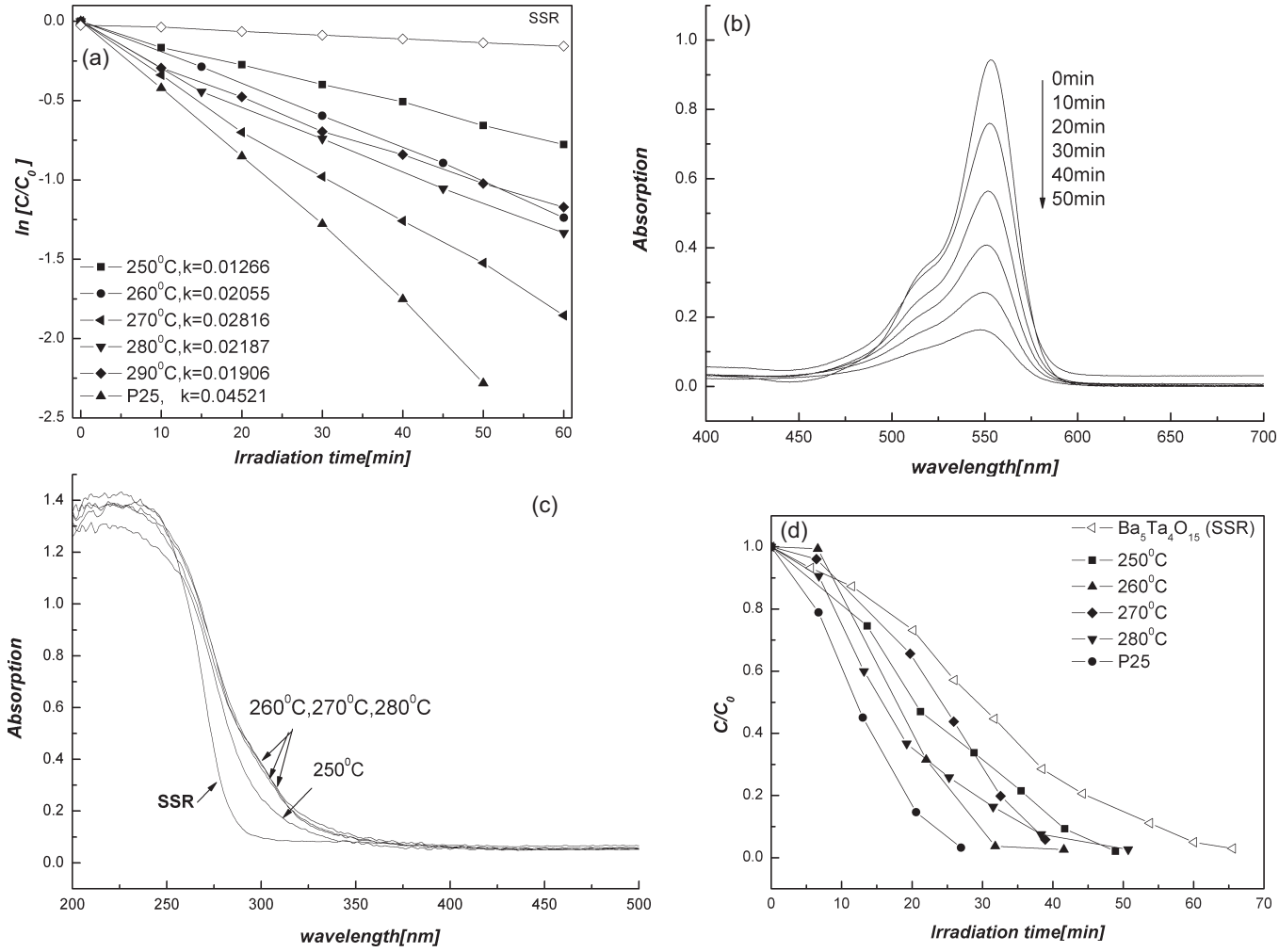

Figure 9. The photocatalytic performance of samples synthesized at various temperatures with a reaction time of 24 h. a) The degradation of RhB, b) degradation curve for RhB (1×10^{-5} M, 200 mL) in the presence of $Ba_5Ta_4O_{15}$ nanosheets (0.100 g) under UV irradiation, c) UV-diffuse reflectance spectra (UV-DRS) of samples obtained at different temperatures, and d) degradation of gaseous formaldehyde (the initial concentration of HCHO is 450 ppm). C/C_0: concentration/initial concentration.

relatively low reaction temperature, although the laser Raman spectroscopy (LRS) studies did reveal the emergence of some crystalline order. For photocatalyst materials with different structures and compositions, the energy structure, such as the conduction band potential, has different effects on the photocatalytic properties, resulting in complicated structure–activity dependencies. The $Ba_5Ta_4O_{15}$ nanosheets obtained at different temperatures (270 and 280 °C) have a similar elemental composition and crystal structure. The absorption edges of the $Ba_5Ta_4O_{15}$ nanosheets are quite similar and the bandgap is estimated to be ca. 3.75 eV for both the samples, which is lower than that of SSR $Ba_5Ta_4O_{15}$ (4.1 eV) (Fig. 9c). One possible reason for the observed differences in the photocatalytic properties of these two samples is that the size of the $Ba_5Ta_4O_{15}$ nanosheets decreases as the reaction temperature is increased, which may lead to a decrease in the number of active sites.

Studies of the luminescence properties of these materials indicate that the closer the bond angle of O–M–O is to 180°, the more the excitation energy is delocalized.[8a,d] The bond angle of O–Ta–O in $Ba_5Ta_4O_{15}$ is quite close to 180°, which results in almost an ideal perovskite structure. This implies that the photogenerated electron–hole pairs in the $Ba_5Ta_4O_{15}$ nanosheets can move relatively easily. The mobility of the electron–hole pairs affects the photocatalytic activity as well as the conduction band level by influencing the probability of the electrons and holes reaching reaction sites on the surface. It is thought that layered structures may promote the generation of photoexcited charges and the separation of the charges without recombination. Compared to bulk tantalates, the laminar structure consists of a monolayer which is only about a unit cell in thickness, and thus a significant proportion of the holes generated inside the crystal can be transferred to the surface and can interact with the organic molecules.[15] Therefore, the $Ba_5Ta_4O_{15}$ nanosheets show enhanced photocatalytic activity.

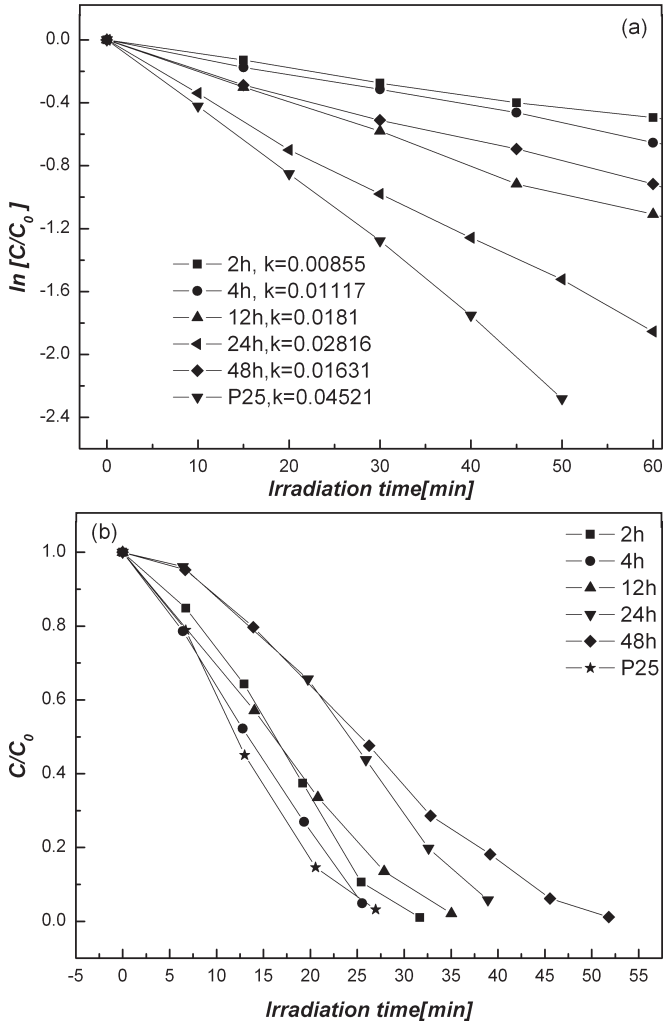

Figure 10. The photocatalytic performance of samples obtained at 270 °C after various reaction times. a) For the degradation of RhB; b) for the degradation of gaseous formaldehyde.

3. Conclusions

Layered perovskite-like single-crystalline $Ba_5Ta_4O_{15}$ nanosheets, with thicknesses approaching unit-cell dimensions, have been synthesized directly using hydrothermal methods. The formation of the $Ba_5Ta_4O_{15}$ nanosheets is seen to be governed by the basicity, temperature, and reaction time. It is thought that the OH^- concentration controls the morphology of the formed $Ba_5Ta_4O_{15}$ nanostructures; $Ba_5Ta_4O_{15}$ nanosheets are formed at higher OH^- concentrations. The formation mechanism of layered $Ba_5Ta_4O_{15}$ nanosheets can be described as a dissolution–recrystallization process (i.e., a dissolution–deposition reaction on the surface of the particles). The monolayer tantalate nanosheets have been shown to exhibit favorable photocatalytic properties for the degradation of RhB and gaseous formaldehyde. The monolayer morphology of the perovskite-like $Ba_5Ta_4O_{15}$ nanosheets allows the electron–hole pairs to easily migrate to the sample surface.

4. Experimental

4.1. Synthesis of $Ba_5Ta_4O_{15}$ Nanosheets

The $Ba_5Ta_4O_{15}$ nanosheets were prepared by a hydrothermal process. All reagents were commercially available and directly used without further purification. The $Ba_5Ta_4O_{15}$ structures were synthesized from a stoichiometric mixture of pure Ta_2O_5 (99.99 %) and $Ba(OH)_2{\cdot}8\,H_2O$ (analytical reagent (AR)). In a typical synthesis process, 1.576 g $Ba(OH)_2{\cdot}8\,H_2O$ was dissolved in water (60 mL), to which 0.884 g of Ta_2O_5 powder was added under stirring. The formed mixture was transferred into a sealed Teflon-lined stainless-steel autoclave with a capacity of 100 mL. After heating the autoclave at 270 °C for 24 h, it was allowed to cool to room temperature. The white product was collected by centrifugation, washed with deionized water three times, and finally dried at 60 °C under vacuum. Other samples were prepared by following a similar procedure under slightly different conditions. All the samples were synthesized at $n_{Ta_2O5} = 0.002$ mol with varying molar ratios of $Ba(OH)_2$ to Ta_2O_5 of 1:2, 1:1, 5:2, and 10:1.

4.2. Characterization

The purity and crystallinity of the as-prepared sample was characterized by XRD on a Bruker D8-advance diffractometer using Cu Kα radiation ($\lambda = 1.5418$ Å). The XRD data for indexing and cell-parameter calculation were collected in scanning mode with a step length of 0.02° and a preset time of 3 s per step. The average crystal size of the $Ba_5Ta_4O_{15}$ powder samples was calculated using the Scherrer equation:

$$Dc = K\lambda/\beta\cos\theta \quad (1)$$

where Dc is the average crystal size, K is the Scherrer constant (equal to 0.89), λ is the X-ray wavelength (0.15418 nm), β is the full width at half maximum (FWHM), and θ is the diffraction angle ($\theta = 32.0°$ was used in this work). The morphologies and structures of the prepared samples were further examined by TEM. Images at low magnification were obtained on a JEOL JEM-1010 instrument operated at an accelerating voltage of 120 kV. High-resolution images and EDX elemental analysis data were obtained on a JEOL JEM-2010 instrument (accelerating voltage: 200 kV). The specimens were prepared by coating a dilute colloidal suspension onto a carbon-coated copper grid. AFM images were obtained on a Nanoscope IIIa microscope (Extended Multimode, Digital Instruments, Santa Barbara, CA). $Ba_5Ta_4O_{15}$ nanosheets were dropped onto a freshly cleaved mica surface, and the surface topography was examined by AFM in tapping mode. A silicon cantilever was used with a resonance frequency of 323 kHz. All the images were obtained using tips with a nominal force constant of 32 N m^{-1} and at a pixel resolution of 512 × 512. Raman measurements were performed using an Instruments Renishaw RM1000 spectrometer with an 1800 grooves mm^{-1} grating. An optical microscope with an 80 × objective was used to focus the 514.5 nm excitation beam from an argon-ion laser. Diffuse reflection spectra (DRS) were obtained on a Hitachi U-3010 UV-vis spectrophotometer.

4.3. Photocatalytic Tests

The photocatalytic degradation of RhB on the $Ba_5Ta_4O_{15}$ nanosheets was carried out in a home-built reactor. A bactericidal lamp (11 W, main wavelength at 254 nm) was used as the light source with an intensity of 1.5 mW cm^{-2}. In each run, 0.10 g of the $Ba_5Ta_4O_{15}$ catalyst was added to 200 mL of the RhB solution (1×10^{-5} mol L^{-1}). After the suspension was premixed for 20 min, the light was turned on to initiate the reaction. The concentration of the RhB solution was monitored using a Hitachi UV-vis spectrophotometer. Gaseous photode-

composition experiments were conducted in an outer-irradiation type quartz cell. 0.05 g $Ba_5Ta_4O_{15}$ powder was homogeneously dispersed on the surface of a glass plate over a 7.5 cm × 2.5 cm area. The glass slide was placed at the bottom of the reaction vessel, perpendicular to the light beam. The distance between the sample and the light source was 5 cm. The vaporized gaseous formaldehyde was forced to flow through the photoreactor. After adsorption equilibrium was reached, the photoreactor was sealed and the photocatalytic reaction was started. Subsequently, the concentration was measured with a SP-502 gas chromatograph (GC).

Received: November 27, 2005
Final version: January 10, 2006

[1] a) T. Sasaki, M. Watanabe, *J. Am. Chem. Soc.* **1998**, *120*, 4682. b) D. M. Kaschak, J. T. Lean, C. C. Waraksa, G. B. Saupe, H. Usami, T. E. Mallouk, *J. Am. Chem. Soc.* **1999**, *121*, 3435. c) T. Sasaki, Y. Ebina, Y. Kitami, M. Watanabe, *J. Phys. Chem. B* **2001**, *105*, 6116. d) N. Miyamoto, T. Nakato, *J. Phys. Chem. B* **2004**, *108*, 6152.

[2] a) A. Hagfeldt, M. Gratzel, *Chem. Rev.* **1995**, *95*, 49. b) M. R. Hoffmann, S. T. Martin, W. Choi, D. W. Bahnemannt, *Chem. Rev.* **1995**, *95*, 735.

[3] a) R. E. Schaak, T. E. Mallouk, *Chem. Mater.* **2000**, *12*, 3427. b) Z. S. Wang, T. Sasaki, M. Muramatsu, Y. Ebina, T. Tanaka, L. Z. Wang, M. Watanabe, *Chem. Mater.* **2003**, *15*, 807. c) T. Tanaka, K. Fukuda, Y. Ebina, K. Takata, T. Sasaki, *Adv. Mater.* **2004**, *16*, 872. d) T. Yui, Y. Mori, T. Tsuchino, T. Itoh, T. Hattori, Y. Fukushima, K. Takagi, *Chem. Mater.* **2005**, *17*, 206. e) S. Z. Chu, S. Inoue, K. Wada, S. Hishita, K. Kurashima, *Adv. Funct. Mater.* **2005**, *15*, 1343.

[4] a) S. Yin, T. Sato, *Ind. Eng. Chem. Res.* **2000**, *39*, 4526. b) M. Yanagisawa, S. Uchida, S. Yin, T. Sato, *Chem. Mater.* **2001**, *13*, 174.

[5] a) G. B. Saupe, C. C. Waraksa, H.-N. Kim, Y. J. Han, D. M. Kaschak, D. M. Skinner, T. E. Mallouk, *Chem. Mater.* **2000**, *12*, 1556. b) R. E. Schaak, T. E. Mallouk, *Chem. Mater.* **2000**, *12*, 3427. c) R. E. Schaak, T. E. Mallouk, *Chem. Mater.* **2002**, *14*, 1455.

[6] a) T. Sasaki, M. Watanabe, *J. Phys. Chem. B* **1997**, *101*, 10159. b) Y. Ebina, T. Sasaki, M. Harada, M. Watanabe, *Chem. Mater.* **2002**, *14*, 4390. c) N. Miyamoto, T. Nakato, *Adv. Mater.* **2002**, *14*, 1267. d) N. Miyamoto, T. Nakato, *J. Phys. Chem. B* **2004**, *108*, 6152.

[7] a) T. Sasaki, M. Watanabe, H. Hashizume, H. Nakazawa, *J. Am. Chem. Soc.* **1996**, *118*, 8329. b) R. E. Schaak, T. E. Mallouk, *Chem. Mater.* **2000**, *12*, 3427. c) M. Yanagisawa, S. Uchida, S. Yin, T. Sato, *Chem. Mater.* **2001**, *13*, 174. d) Y. Ebina, T. Sasaki, M. Harada, M. Watanabe, *Chem. Mater.* **2002**, *14*, 4390. e) T. Sasaki, Y. Ebina, Y. Kitami, M. Watanabe, *J. Phys. Chem. B* **2001**, *105*, 6116. f) A. Takagaki, M. Sugisawa, D. Lu, J. N. Kondo, M. Hara, K. Domen, S. Hayashi, *J. Am. Chem. Soc.* **2003**, *125*, 5479.

[8] a) K. Sayama, H. Arakawa, K. Domen, *Catal. Today* **1990**, *28*, 175. b) H. Kato, A. Kudo, *Chem. Phys. Lett.* **1998**, *295*, 487. c) H. G. Kim, D. W. Hwang, J. D. Kim, Y. G. Kim, J. S. Lee, *Chem. Commun.* **1999**, 1077. d) A. Kudo, H. Kato, S. Nakagawa, *J. Phys. Chem. B* **2000**, *104*, 571. e) H. Kato, K. Asakura, A. Kudo, *J. Am. Chem. Soc.* **2003**, *125*, 3082. f) H. Kato, A. Kudo, *Catal. Today* **2003**, *78*, 561.

[9] a) P. S. Doba, R. S. Katiyar, Y. Jiang, R. Guo, A. S. Bhalla, *J. Raman Spectrosc.* **2000**, *31*, 1061. b) G. Yang, Y. Kong, W. H. Hou, Q. J. Yan, *J. Phys. Chem. B* **2005**, *109*, 1371.

[10] W. J. Li, E. W. Shi, W. Z. Zhong, Z. W. Yin, *J. Cryst. Growth* **1999**, *203*, 186.

[11] a) J. F. Banfield, S. A. Welch, H. Z. Zhang, T. T. Ebert, R. L. Penn, *Science* **2000**, 289, 751. b) R. L. Penn, J. F. Banfield, *Geochim. Cosmochim. Acta* **1999**, *63*, 1549.

[12] Y. Hakuta, H. Ura, H. Hayashi, K. Arai, *Ind. Eng. Chem. Res.* **2005**, *44*, 840.

[13] a) S. H. Yu, B. Liu, M. S. Mo, J. H. Huang, X. M. Liu, Y. T. Qian, *Adv. Funct. Mater.* **2003**, *13*, 639. b) T. Sasaki, Y. Ebina, Y. Kitami, M. Watanabe, *J. Phys. Chem. B* **2001**, *105*, 6116. c) J. C. Yu, A. W. Xu, L. Z. Zhang, R. Q. Song, L. Wu, *J. Phys. Chem. B* **2004**, *108*, 64.

[14] X. Zhang, R. Frech, *Electrochim. Acta* **1998**, *43*, 861.

[15] a) C. Zhang, Y. F. Zhu, *Chem. Mater.* **2005**, *17*, 3537. b) H. B. Fu, C. S. Pan, W. Q. Yao, Y. F. Zhu, *J. Phys. Chem. B* **2005**, *109*, 22432. c) H. Otsuka, K. Y. Kim, A. Kouzu, I. Takimoto, H. Fujimori, Y. Sakata, H. Imamura, T. Matsumoto, K. Toda, *Chem. Lett.* **2005**, *34*, 822.